

A Universal Urbach Rule for Disordered Organic Semiconductors

Christina Kaiser, Oskar J. Sandberg*, Nasim Zarrabi, Wei Li, Paul Meredith, Ardalan Armin*

Sustainable Advanced Materials (Sêr-SAM), Department of Physics, Swansea University, Singleton Park, Swansea SA2 8PP, United Kingdom

*Email: ardalan.armin@swansea.ac.uk; o.j.sandberg@swansea.ac.uk

Abstract

In crystalline semiconductors, absorption onset sharpness is characterized by temperature dependent Urbach energies. These energies quantify the static, structural disorder causing localized exponential-tail states, and dynamic disorder from electron-phonon scattering. Applicability of this exponential-tail model to disordered solids has been long debated. Nonetheless, exponential fittings are routinely applied to sub-gap absorption analysis of organic semiconductors. Herein, we elucidate the sub-gap spectral line-shapes of organic semiconductors and their blends by temperature-dependent quantum efficiency measurements. We find that sub-gap absorption due to singlet excitons is universally dominated by thermal broadening at low photon energies and the associated Urbach energy equals the thermal energy, regardless of static disorder. This is consistent with absorptions obtained from a convolution of Gaussian density of excitonic states weighted by Boltzmann-like thermally activated optical transitions. A simple model is presented that explains absorption line-shapes of disordered systems, and we also provide a strategy to determine the excitonic disorder energy. Our findings elaborate the meaning of the Urbach energy in molecular solids and relate the photo-physics to static disorder, crucial for optimizing organic solar cells for which we present a new radiative open-circuit voltage limit.

Introduction

Recently, research on organic solar cells has seen significant progress through the development of non-fullerene electron acceptors (NFAs), in particular delivering increases in single-junction efficiencies from 13.1 to 18.7 % between 2017 to 2021.^{1,2} This has revived ambitions to ultimately achieve industrial scale low-cost photovoltaics with low embodied manufacturing energy. While chemists have been productively synthesising new materials, understanding of the opto-electronic properties lags behind – particularly in relation as to why these new NFA blends are so effective at photogeneration with low voltage losses. A particular area of intense interest is light absorption and how it is related to molecular

dipole moments and their energetic disorder. Of course, this is also a very relevant question for the fundamental solid-state physics of molecular and disordered semiconductors. Furthermore, energetic disorder critically determines dominant radiative loss mechanisms limiting the open-circuit voltage in optoelectronic applications.

In general, semiconductors tend to absorb light at photon energies below the bandgap (sub-gap absorption) depending on the energetic disorder. In the case of inorganic semiconductors, the absorption coefficient (α) often displays an exponential tail below the bands. These so-called Urbach tails increase their broadening with temperature T .³ The sub-gap α generally follows the expression

$$\alpha(E, T) \propto \exp\left(\frac{E - E_{\text{on}}(T)}{E_{\text{U}}(T)}\right), \quad (1)$$

where E is the photon energy, E_{on} is the energy onset of the tail, and $E_{\text{U}}(T)$ is the Urbach energy quantifying the total energetic disorder of the system. Depending on the semiconductor, E_{U} generally varies between 10 to 100 meV at room temperature.⁴⁻⁷ In banded semiconductors, it has been suggested that $E_{\text{U}}(T) = E_{\text{U,D}}(T) + E_{\text{U,S}}$, where $E_{\text{U,D}}(T)$ is a temperature-dependent dynamical disorder term related to the thermal occupation of phonon states,^{4,8} while $E_{\text{U,S}}$ is the width of the assumed exponential distribution of sub-gap states induced by static disorder.⁹ However, a unifying theory describing the density of states and their absorption leading to Urbach tails for materials of different chemical bonding and morphology is still lacking.¹⁰⁻¹²

In non-excitonic amorphous semiconductors, the definition of a clear bandgap edge is often difficult due to large static disorder inducing sub-gap broadening. Organic semiconductors, which are excitonic and partially amorphous, display even more complex sub-gap features including intermolecular hybrid charge transfer (CT) states in technologically-relevant blends of electron donors (D) and acceptors (A), excitonic features¹³ and trap states¹⁴. CT states give rise to light absorption with Gaussian sub-gap spectral line-shapes. This has been attributed to intermolecular D:A transitions described by non-adiabatic Marcus theory¹⁵ or its extensions¹⁶⁻¹⁹, suggesting that the static disorder is governed by a Gaussian distribution of CT states. Whether a similar description applies for sub-gap absorption by intramolecular excitons is unclear. With the rise of NFA semiconductors with small energetic offset relative to donors²⁰, the lack of CT state sub-gap spectral features in donor-acceptor blends has led to the increased usage of Urbach energies to understand disorder and sub-gap photo-physics. As a rule of thumb, it has been assumed that low Urbach energies are indicative of lower static disorder and hence expected to result in higher performance such as reduced charge recombination and higher charge carrier mobilities in a photovoltaic device.²¹⁻²³ Due to the complex and often convoluted spectral features in sub-gap light absorption of organic semiconductors, however, the Urbach energy carries significant ambiguity. Moreover, a long-standing debate²⁴⁻²⁶ on the distribution of density of states (DOS) defining the static disorder in organic semiconductors has been revived: does the DOS follow a

Gaussian or an exponential distribution? With no doubt, the origin of the static disorder is of great importance for the classification and future development of organic semiconductors and their electro-optical properties. However, it has remained unclear how this important figure-of-merit relates to the Urbach energy.

In this work, we show that the exciton sub-gap absorption in organic semiconductors, at photon energies well below the gap, is generally characterized by Urbach tails with characteristic energies equivalent to the thermal energy kT as demonstrated by temperature-dependent EQE measurements. However, these Urbach tails are often convoluted with Gaussian line-shapes induced by trap states and/or CT states, resulting in erroneous, energy-dependent, Urbach energies larger than kT . A simple model, combining the Gaussian distributed DOS with Boltzmann-like thermally activated optical transitions, is shown to reproduce the absorption profiles and to give an estimate for the Gaussian static disorder. Based on this model, the exciton sub-absorption is found to be composed of two regimes: near the onset, the sub-gap absorption is dominated by Gaussian static disorder resulting in strongly energy dependent Urbach energies, while thermal broadening dominates at energies well below the gap, where the Urbach energy approaches kT . As such, using an (energy-independent) Urbach energy as a probe for the static disorder in organic solar cells is meaningless. Finally, the effect of exciton static disorder and thermal broadening on the expected radiative voltage losses and power conversion efficiency (PCE) in organic solar cells based on low offset D:A blends is clarified.

Results and Discussion

The spectral line-shape of α and the absorbance A in the sub-gap tail are generally related via a modified Beer-Lambert law, $A = \tilde{f}\alpha d$, where d is the thickness of the active layer and \tilde{f} is an energy-dependent correction factor accounting for optical interference.^{27,28} For optically thin films with layer thicknesses of 100 to 150 nm, \tilde{f} is often assumed to be close to 1 (negligible optical interference effects). Moreover, it has been shown for efficient D:A systems that the internal quantum efficiency (IQE) is generally excitation energy independent, hence $\text{EQE} \propto A$ and the spectral line shape of the EQE follows α .²⁹⁻³² Based on this underlying premise, EQE measurements have been frequently employed in the past to determine E_U . However, a previous lack of sensitivity in the EQE measurements has led to speculative assumptions about the spectral range of trap state absorptions, exponential tails and associated E_U in organic semiconductors. By choosing a small fitting range, exponential fits can be forced on to EQE spectra resulting in rather arbitrary E_U dependent on the spectral range of the fitting. More insight can instead be gained from the apparent Urbach energy (E_U^{app}) here defined as:

$$E_U^{\text{app}}(E) = \left[\frac{d \ln(\text{EQE})}{dE} \right]^{-1} \quad (2)$$

For a true exponential tail of the form eq. 1, E_U^{app} is constant in the sub-gap spectral region and given by E_U .

Determination of the apparent Urbach energy in organic solar cells. Figure 1 shows the EQE and E_U^{app} for a wide range of organic semiconductor D:A blends. The material systems studied here can be generally grouped according to the D:A energy offset or, in other words, the difference between the CT state energy E_{CT} and the optical bandgap E_{opt} . Here, E_{opt} is typically equal to the local exciton (LE) energy of the lower-bandgap component (between D and A). Large offset systems, such as PCDTBT:PC₇₀BM, BQR:PC₇₀BM and PBDB-T:PC₇₀BM (Figure 1a), show three distinct spectral ranges for energies below the gap: (i) mid-gap trap state absorption at energies below 1.2 eV, (ii) CT state absorption in the mid-range (~1.2 – 1.5 eV) and (iii) LE absorption above 1.5 eV. For mid-gap and CT state absorption, Gaussian-shaped EQE features are observed.¹⁴ These features are consistent with Marcus charge-transfer between states that are distributed in accordance with a Gaussian density of sub-gap states. Details of the Gaussian fits are provided in the **Methods section**. Because of the Gaussian line-shape (see eq. S7), the corresponding E_U^{app} in the spectral range of CT absorption is expected to be strongly energy-dependent and given by $E_U^{\text{app}} \approx 2kT\lambda_{\text{CT}}/(E_{\text{CT}} + \lambda_{\text{CT}} - E)$; this is highlighted by the black solid line in Figure 1a. Here, E_{CT} and λ_{CT} , as obtained from the Gaussian fits, are to be considered the effective energy and reorganization energy of CT states which includes the effect of static disorder (see **Supplementary Information**).^{16,18} At higher energies corresponding to the sub-gap LE absorption regime, in turn, E_U^{app} has a narrow parabolic shape with a sharp minimum at roughly 40 - 50 meV for the large offset blends.

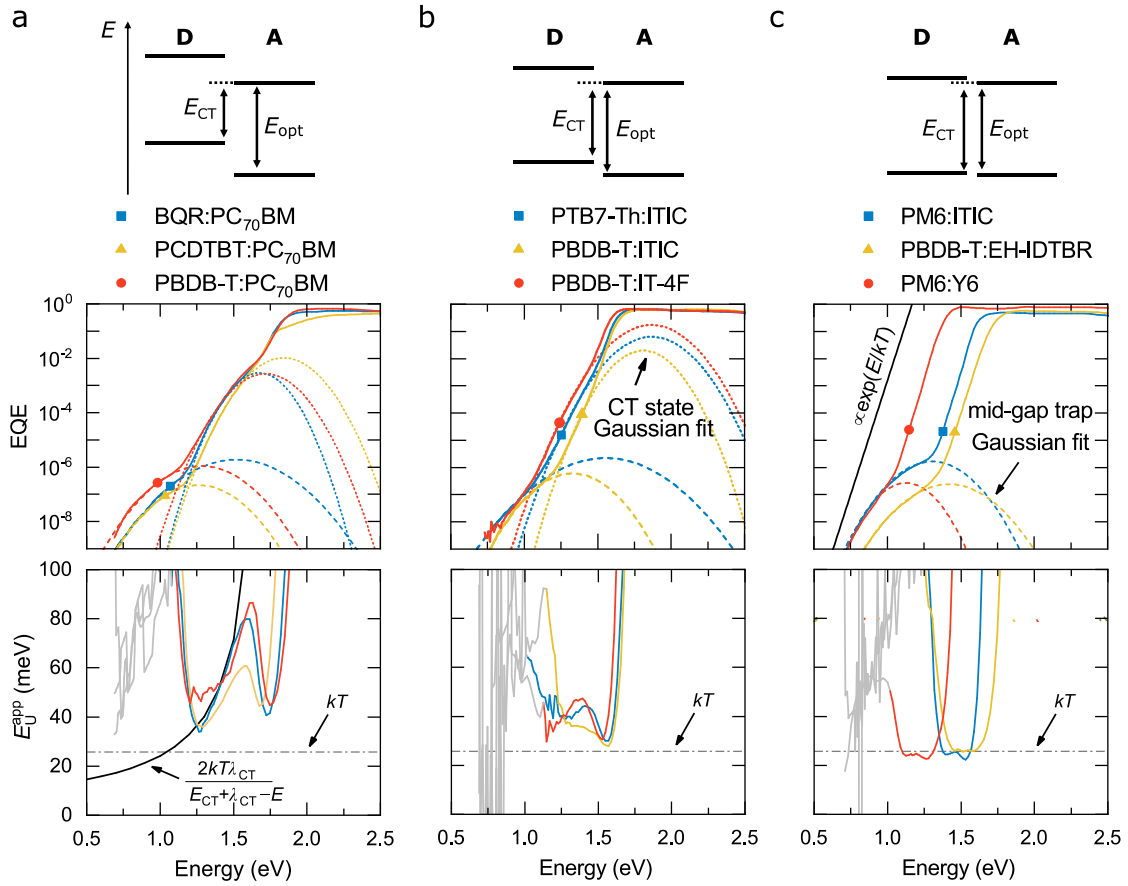


Figure 1 | EQE and E_U^{app} for organic D:A blends with different energetic offsets between E_{CT} and E_{opt} . Schematic illustration of the energetic offset ($E_{\text{opt}} - E_{\text{CT}}$) decreasing from left to right. Gaussian fits in the spectral range of CT state and trap state absorption are performed where possible. For low offset blends PM6:Y6, PM6:ITIC and PBDB-T:EH-IDTBR, the EQE tail has the form $e^{E/kT}$, and E_U^{app} roughly equals kT in the spectral range that is dominated by the absorption of the acceptor. For large offset material systems, such as BQR:PC₇₀BM, PBDB-T:PC₇₀BM and PCDTBT:PC₇₀BM, E_U^{app} shows a $2kT\lambda_{\text{CT}}/(E_{\text{CT}} + \lambda_{\text{CT}} - E)$ dependence in the spectral range of CT absorption.

The EQE and E_U^{app} of blends with a smaller offset between E_{CT} and E_{opt} (PTB7-Th:ITIC, PBDB-T:ITIC and PBDB-T:IT-4F) are shown in the Figure 1b. In this case, the Gaussian CT state line-shape is barely recognizable, and the α tail in the spectral range of LEs is visible over a wider spectral range. While E_U^{app} retains its parabolic shape in the LE sub-gap absorption regime, because of the wider range, the minimum value of E_U^{app} is significantly reduced to values close to kT . Finally, the EQE and E_U^{app} of blends in low-offset D:NFA systems (PM6:Y6, PM6:ITIC and PBDB-T:EH-IDTBR) are shown in Figure 1c. In these blends, the CT state absorption can no longer be discerned from the EQE spectra. Instead, the α tail in the spectral range of LEs remains dominant down to the energy range of mid-gap

state excitation. In this limit, the E_U^{app} in the LE-dominated sub-gap absorption range finally saturates and reaches a broad plateau where $E_U^{\text{app}} \approx kT$.

The above experimental observation for low offset D:NFA systems suggests the presence of an intramolecular sub-gap absorption regime where $\alpha \propto \exp(E/kT)$, but that its spectroscopic observation is obstructed by CT absorption in systems with larger offsets. To further clarify this, neat D or A systems (lacking the D-A CT absorption feature in the sub-gap EQE spectrum) were investigated as shown in **Figure 2**. In the case of neat PC₇₀BM (Figure 2a), a narrow spectral range where $E_U^{\text{app}} \approx kT$ can be identified. This range is limited by deep trap-state absorption at low energies, while the poor exciton dissociation in the neat phase (translating into a low IQE) strongly reduces the EQE range at higher energies. However, the spectral range where $E_U^{\text{app}} \approx kT$ can be increased by adding 0.1 mol% of the wide-gap donor m-MTDATA, resulting in enhanced exciton dissociation. Since m-MTDATA:PC₇₀BM is characterized by a low E_{CT} , the LE tail of PC₇₀BM can be clearly distinguished from CT states as shown in Figure 2a.³³ By further increasing the donor content, the CT state absorption increases and the parabolic shape of E_U^{app} emerges. This explains the parabolic shapes seen for large offset systems in Figure 1a, which appear when the α tail in the spectral range of LE absorption becomes convoluted with CT state absorption. This is further supported by results shown in Figure 2b for neat NFA devices comprising ITIC and IT-4F active layers, respectively. Here again, exponentially decaying α tail regions with $E_U^{\text{app}} \approx kT$ are observed.

To check if $E_U^{\text{app}} \approx kT$ is also true for donor materials has proven more challenging, since the neat donor absorption is often convoluted with deep trap-state absorption. This convolution effectively increases E_U^{app} above kT as shown for PBDB-T in Figure 2c, where $E_U^{\text{app}} \approx 30$ meV. The problem can be circumvented by using narrow-gap polymer donors such as PBTQ(OD) or PTTBAI, which show strongly redshifted EQE spectra when blended with PC₇₀BM as previously reported.³⁴ As shown in Figure 2c, E_U^{app} is around 22 meV in this case. While deviations of the type $E_U^{\text{app}} > kT + 10$ meV are due to the presence of other absorbing species like CT states or deep trap states, small deviations of E_U^{app} around kT are likely caused by interference effects, i.e. non-constant \tilde{f} , as shown previously.^{27,35} Interference effects arise from the spectral dependence of the optical constants of the different layers in the thin-film stack and generally vary with the thickness of the active layer. To demonstrate the presence of interference effects, we therefore fabricated PM6:ITIC devices and PM6:Y6 devices of different active layer thicknesses. Indeed, as illustrated in the **Figures S3**, E_U^{app} shows a weak thickness dependence leading to deviations around kT from +2.3 meV to -5.8 meV. The thickness dependence of E_U^{app} is further corroborated by optical transfer-matrix simulations (see **Figure S4** in the **Supplementary Information**).

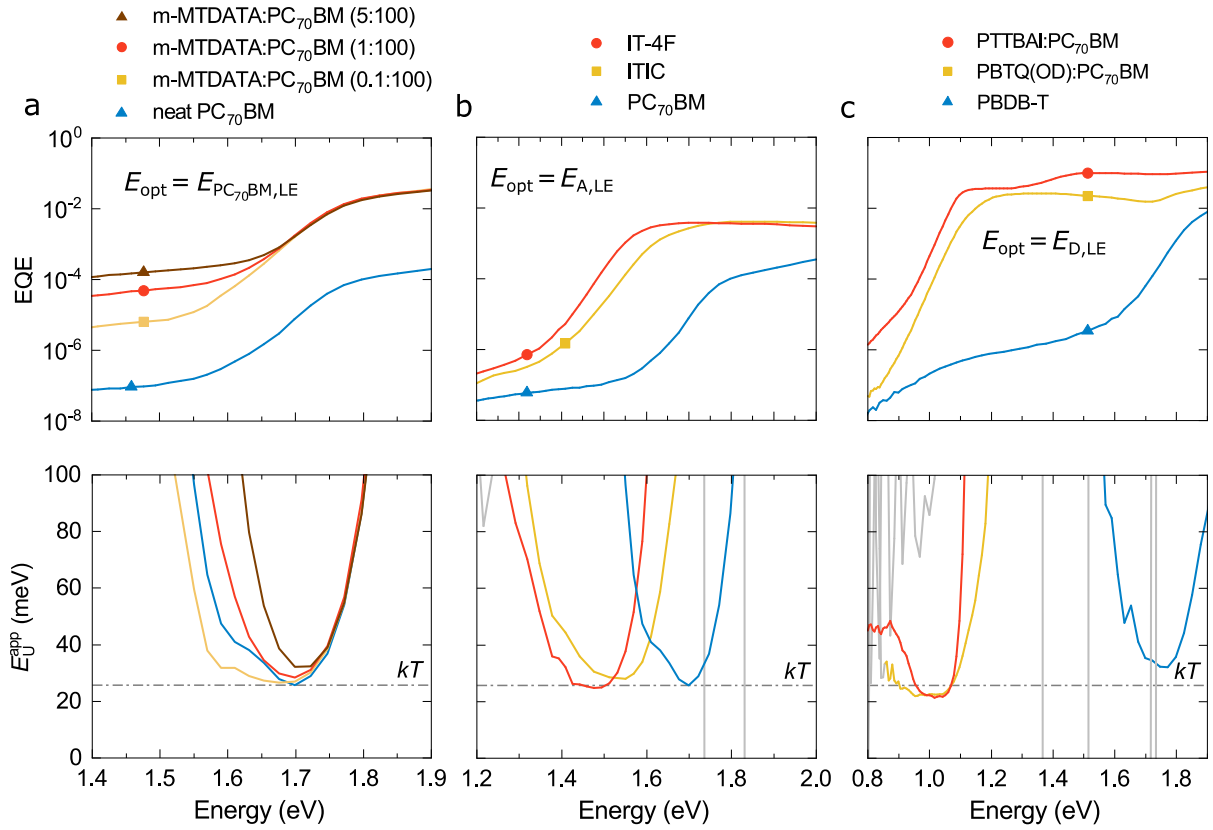


Figure 2 | EQE tail dominated by neat material absorption. **a**, EQE and E_U^{app} for a series of m-MTDATA sensitized PC₇₀BM solar cells. The widest energy range over which E_U^{app} equals kT is observed for 0.1 mol% m-MTDATA in PC₇₀BM due to improved exciton dissociation in comparison to neat PC₇₀BM. Examples for EQE tails partially dominated by **b**, the neat donor absorption or by **c**, the neat acceptor absorption hence showing $E_U^{\text{app}} \approx kT$ in some parts of the spectrum. EQE spectra of PTTBAI:PC₇₀BM and PBTQ(OD):PC₇₀BM are taken from reference 34.

Temperature-dependent EQE measurements. To verify that the exponential α tails in the spectral range of LEs are characterized by $E_U^{\text{app}} \approx kT$, we performed T -dependent EQE measurements on PBDB-T:EH-IDTBR, PM6:Y6 and PM6:ITIC, and the neat materials IT-4F and Y6. **Figure 3a** shows the normalized EQE and the respective E_U^{app} spectra of three representative systems: PBDB-T:EH-IDTBR, PM6:Y6 and IT-4F. The remaining material systems are provided in the **Supplementary Information**. Depending on T , two different regimes can be distinguished in the sub-gap absorption tail: At high T , E_U^{app} spectra show a T -dependent plateau only influenced by interference effects and the shift in the absorption onset. At low T , however, the E_U^{app} spectra generally attain a parabolic shape suggesting that the LE tail becomes convoluted with CT and/or mid-gap states. The thermal activation of the exponential α tail is then finally illustrated in **Figure 3b** where E_U^{app} (at a constant energy) in the plateau region is shown as a function of kT for the systems studied. We see that E_U^{app} at higher

temperature is linear and equals $kT \pm 2.5$ meV, where the offset arises from interference effects. At lower T , E_U^{app} eventually deviates from linearity, as the spectral shape is increasingly affected by other absorbing species. For example, the low-energy tail of the CT absorption may emerge at low T owing to its distinctly different T -dependence compared to LE absorption.³⁶ Moreover, the absorption of trap states is expected to play a role as well, while little is yet known about their spectral broadening as a function of T .

For comparison, we also measured T -dependent EQE spectra of a commercial a-Si:H thin-film solar cell (EQE and E_U^{app} spectra shown in **Figure S6**). In banded semiconductors such as a-Si:H, the total energetic disorder is $E_U(T) = E_{U,D}(T) + E_{U,S}$, consistent with the presence of an exponential DOS of tail states (defined by the associated width $E_{U,S}$). In **Figure 3b**, two regimes can be distinguished for a-Si:H comprising the low-temperature saturation of E_U to $E_U(0) \approx 40$ meV and thermal activation at higher temperatures with an offset of roughly 21 meV from kT in agreement with previous reports.^{37–39} In contrast, for the organic semiconductor systems in **Figure 3b**, an extrapolation to $T = 0$ implies that $E_{U,S} \approx 0$, suggesting the lack of an exponential tail state distribution in these systems. These observations raise the question why excitons in organic semiconductors follow $\alpha \propto \exp(E/kT)$ resulting in $E_U^{\text{app}} \approx kT$ and what is the role of static disorder in shaping the E_U^{app} spectra.

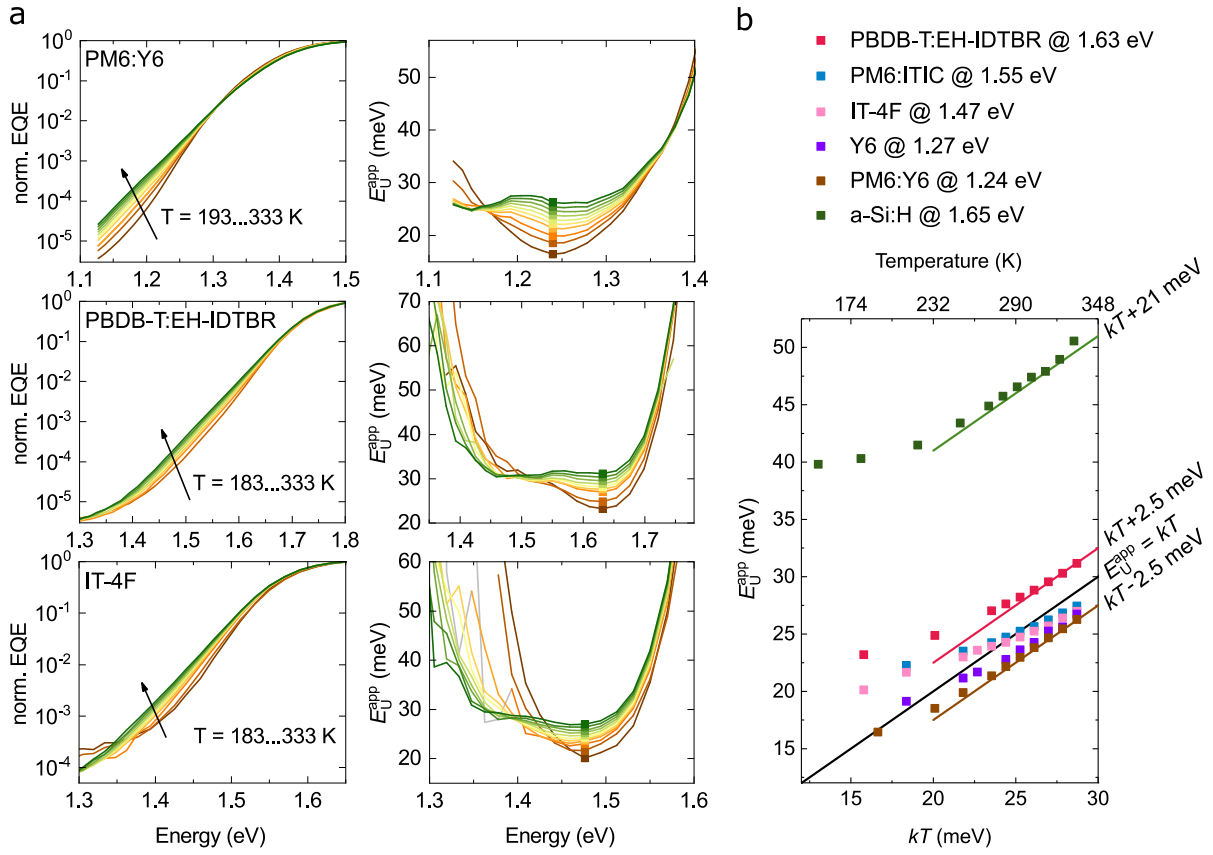


Figure 3 | Temperature dependent apparent Urbach energies. **a**, Normalized sub-gap EQE and E_U^{app} spectra of inverted PM6:Y6, PBDB-T:EH-IDTBR and neat IT-4F solar cells at different temperatures. Independent of temperature, E_U^{app} spectra show a local minimum (solid markers) at a constant energy within the spectral range dominated by exciton absorption. **b**, Minimum E_U^{app} as a function of kT for all tested materials systems including a commercial a-Si:H thin-film solar cell.

Model for understanding the sub-gap α . In the context of the Marcus formalism for non-adiabatic charge transfer (high-temperature limit), the presence of $E_U^{\text{app}} \approx kT$ in the spectral range of LE absorption (described by the absorption coefficient α_{LE}) may be rationalized in terms of non-equal potential energy surfaces for the excited state and the ground state. By assuming a significantly more diffuse or delocalized excited state, compared to the (strongly localized) ground state, a much smaller reorganization energy is obtained for the excited state in comparison to the ground state.^{40–42} In this limit, we expect $\alpha_{\text{LE}}(E) \approx \alpha_{\text{sat}} \exp([E - E_{\text{opt}}]/kT)$ for $E < E_{\text{opt}}$, in the case of negligible static disorder (see **Supplementary Information**). Here, α_{sat} includes a $1/E$ dependence, however, the sub-gap spectral line-shape is dominated by the Boltzmann factor. For above-gap absorption $E > E_{\text{opt}}$, we assume $\alpha_{\text{LE}}(E) \approx \alpha_{\text{sat}}$. We note that this simplification of $\alpha_{\text{LE}}(E)$ essentially follows a Miller-Abrahams-type charge-transfer formalism, sometimes used to describe exciton migration⁴³, but more commonly used for charge transport⁴⁴ in organic semiconductors. Accounting for static disorder described by a DOS given by $g_{\text{DOS}}(E'_{\text{opt}})$, the total absorption coefficient is of the form $\alpha_{\text{LE}}(E) =$

$\int \alpha_{\text{LE}}(E, E'_{\text{opt}}) g_{\text{DOS}}(E'_{\text{opt}}) dE'_{\text{opt}}$. In the **Supplementary Information**, expressions for the associated absorption coefficients are derived for the cases of a Gaussian DOS and an exponential tail DOS. For the case of an exponential tail DOS with the width W , we obtain $E_{\text{U}}^{\text{app}} = W$ (see **Figure S7**). This is indeed not what we observe in experiments. For a Gaussian DOS, in turn, we obtain α in the form

$$\frac{\alpha_{\text{LE}}(E)}{\alpha_{\text{sat}}} = \frac{1}{2} \left\{ \exp\left(\frac{E - E_{\text{opt}} + \frac{\sigma_s^2}{2kT}}{kT}\right) \left[1 - \text{erf}\left(\frac{E - E_{\text{opt}} + \frac{\sigma_s^2}{kT}}{\sigma_s \sqrt{2}}\right) \right] + \text{erf}\left(\frac{E - E_{\text{opt}}}{\sigma_s \sqrt{2}}\right) + 1 \right\} \quad (3)$$

where σ_s is the standard deviation of the Gaussian DOS and E_{opt} is the associated mean exciton energy. Here, E_{opt} corresponds to the optical gap and is determined by the first excited singlet state of either donor ($E_{\text{opt}} = E_{\text{D,LE}}$) or acceptor ($E_{\text{opt}} = E_{\text{A,LE}}$) in a blend. For $E \ll E_{\text{opt}}$, eq. (3) reduces to the exponential part and $E_{\text{U}}^{\text{app}}$ therefore equals kT . For $E \geq E_{\text{opt}}$, the error functions govern the spectral shape at the absorption edge as demonstrated in **Figure S8** in the **Supplementary Information**.

To validate the model, we applied eq. (3) to T -dependent EQE spectra, as demonstrated in **Figure 4a** for neat Y6 and IT-4F. Using neat materials avoids the influences of CT states in the low-energy tail although trap states are always present at lower energies. Doing so, we obtain σ_s values of 47.0 ± 0.7 meV for Y6 and 35.0 ± 2.6 meV for IT-4F (see **Figure S10** in the **Supplementary Information**). More fittings on room temperature EQE spectra of other material systems are shown in the **Figure S11** in the **Supplementary Information**. For blend systems, the full experimental sub-gap EQE can be reconstructed assuming $\alpha(E) = \alpha_{\text{LE}}(E) + \alpha_{\text{CT}}(E) + \alpha_{\text{t}}(E)$ constituting the exponentially decaying α_{LE} according to eq. (3) and the sum of two Gaussian functions (CT states and deep trap states; see eq. 5). In **Figure 4b**, we demonstrate the model for PBDB-T:PC₇₀BM using the parameters $E_{\text{opt}} = 1.89$ eV and $\sigma_s = 60$ meV, and other Gaussian fit parameters summarized in **Table S1** in the **Supplementary Information**. PBDB-T:PC₇₀BM belongs to the group of blends for which $E_{\text{CT}} \ll E_{\text{opt}}$ with $E_{\text{CT}} - E_{\text{opt}} \approx 0.45$ eV. Nevertheless, the simplified model reproduces the strong spectral dependence of the experimental $E_{\text{U}}^{\text{app}}$, including the parabolic behaviour in the LE absorption dominated spectral range. On the other hand, by keeping all other parameters constant while increasing E_{CT} with respect to E_{opt} , the emergence of the $E_{\text{U}}^{\text{app}} = kT$ plateau at around 1.6 ± 0.1 eV can be reproduced.

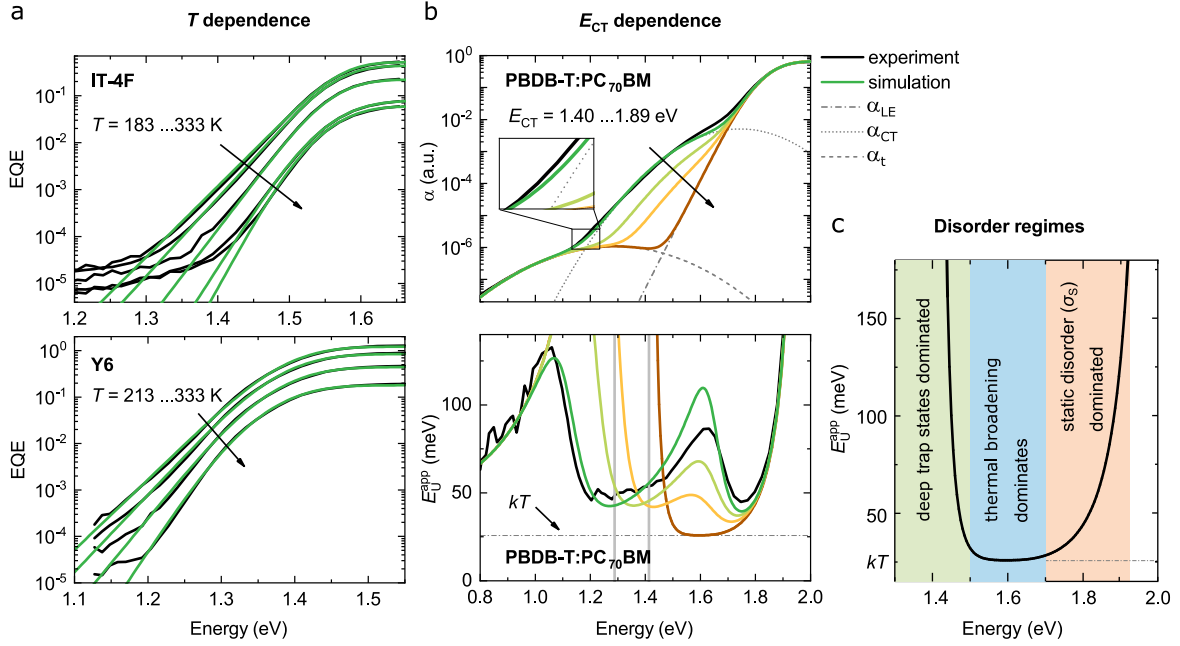


Figure 4 | The sub-bandgap EQE as a function of T and E_{CT} . **a**, Experimental (black lines) and simulated (green lines) sub-gap EQE spectra of IT-4F and Y6. **b**, The line-shape of the experimental sub-gap EQE of PBDB-T:PC₇₀BM can be described as the sum of LE absorption, CT state absorption, and trap state absorption: $\alpha = \alpha_{LE} + \alpha_{CT} + \alpha_t$, with α_{LE} given by eq. 3 ($E_{opt} = 1.89$ eV, $\sigma_s = 60$ meV), while α_{CT} and α_t are determined from their respective Gaussian fits. In the experiment, E_U^{app} is well above kT , since $E_{opt} - E_{CT} > 0.3$ eV. Increasing E_{CT} (see eq. 5) in the simulation results in $E_U^{app} \rightarrow kT$ between 1.5 to 1.7 eV. **c**, Schematic representation of the disorder regimes dominating α in the absence of CT absorption comprising (i) static disorder σ_s close to the band edge, (ii) thermal broadening, where $E_U^{app} = kT$, and (iii) deep trap state absorption well below the gap.

In the absence of CT states, the above model predicts three sub-gap regimes of the $\alpha(E)$ based on the dominant disorder mechanism as illustrated in **Figure 4c**. For photon energies close to the gap ($E > E_{opt} - \sigma_s^2/kT$), E_U^{app} is dominated by (Gaussian) static disorder. In this regime, the absorption resembles a Gaussian-like shape, where the steepness close to the gap is determined by σ_s , causing a redshift of the effective energy gap with increasing σ_s . While E_U^{app} does not directly represent σ_s at any energy, a positive correlation between E_U^{app} and σ_s is observed in this regime (see **Figure S9**). A closer inspection suggests that E_U^{app} is strongly energy dependent in this regime, scaling with σ_s as $E_U^{app}(E) \approx 2\sigma_s^2/(E_X - E)$, for $\sigma_s < 4kT$, where E_X is a constant independent of E . This explains the previously reported correlation between morphological disorder and E_U^{app} close to the absorption onset.^{22,45-47} For $E < E_{opt} - \sigma_s^2/kT$, however, the exponential term in eq. (3) eventually starts to dominate the spectral line shape of α_{LE} . In this regime, the sub-gap absorption of LEs is dominated by thermal broadening with $E_U^{app} \rightarrow kT$, thus becoming independent of σ_s . The transition between the static disorder dominated and the thermal broadening dominated regime depends on σ_s (which is a

measure of the Gaussian static disorder) and the temperature. This is simulated for the two cases $\sigma_s = 70$ meV and $\sigma_s = 100$ meV as shown in **Figure S9**: For $\sigma_s = 70$ meV, E_U^{app} reaches kT at $\alpha(E)$ values 3 to 4 orders of magnitudes below α_{sat} , while this is 6 orders below α_{sat} for $\sigma_s = 100$ meV at room temperature. Finally, at energies well below the optical gap, $\alpha(E)$ eventually becomes dominated by deep trap state absorption, resulting in an artificial increase in E_U^{app} and a concomitant deviation from $E_U^{\text{app}} = kT$. Deep trap state absorption is typically observed 6 orders of magnitude below α_{sat} limiting the spectral range dominated by thermal broadening.

Based on these considerations, we estimate that it is possible to observe $E_U^{\text{app}} \approx kT$ only when $\sigma_s < 100$ meV (see Figure S9). Other conditions that must be met are: (i) the neat phase absorption of one component is spectrally separated from the other neat phase absorption, as well as from the CT states and trap states; (ii) the dynamic range of the EQE (or α) measurement is sufficiently wide to measure photocurrent at wavelengths well below the absorption onset of the neat material ($E < E_{\text{opt}} - \sigma_s^2/kT$); and (iii) optical cavity effects are not significant. Exponential sub-gap EQE spectra previously reported in literature for BHJs often do not fulfill these requirements, explaining reported Urbach energies much larger than kT . Importantly, the E_U^{app} spectra introduced here do not suffer from the short fitting ranges of previous of E_U measurements. In contrast, we have shown that an exponential distribution of tail states cannot explain the sub-gap spectral line-shape associated with singlet absorption, nor CT or trap state absorption in organic semiconductors.

Recombination losses and the radiative V_{OC} limit set by excitons. The presence of sub-gap absorption is known to induce radiative recombination losses additional to those predicted by Shockley and Queisser (SQ) approach. While the short-circuit current density (J_{SC}) remains largely unaffected, the presence of sub-gap absorption mainly translates into enhanced losses in the open-circuit voltage (V_{OC}). In general, the V_{OC} can be expressed as $V_{\text{OC}} = V_{\text{OC}}^{\text{SQ}} - \Delta V_{\text{OC}}^{\text{RAD}} - \Delta V_{\text{OC}}^{\text{NR}}$, where $V_{\text{OC}}^{\text{SQ}}$ represents the upper thermodynamic limit of the V_{OC} based on the SQ model, assuming perfect above-gap absorption and no sub-gap absorption. Furthermore, $\Delta V_{\text{OC}}^{\text{RAD}} = V_{\text{OC}}^{\text{SQ}} - V_{\text{OC}}^{\text{RAD}}$ is the radiative loss induced by sub-gap absorption, while $\Delta V_{\text{OC}}^{\text{NR}} = V_{\text{OC}}^{\text{RAD}} - V_{\text{OC}}$ is the non-radiative loss. Here, $V_{\text{OC}}^{\text{RAD}}$ is the radiative limit of the V_{OC} corresponding to the expected V_{OC} in the absence of non-radiative losses. In accordance with detailed balance, we expect $V_{\text{OC}}^{\text{RAD}} = \frac{kT}{q} \ln \left(\frac{J_{\text{SC}}}{J_0^{\text{RAD}}} + 1 \right)$, where $J_{\text{SC}} = q \int_0^\infty \text{EQE}(E) \Phi_{\text{sun}}(E) dE$ and $J_0^{\text{RAD}} = q \int_0^\infty \text{EQE}(E) \Phi_{\text{BB}}(E) dE$ is the dark saturation current density in the radiative limit; q is the elementary charge and Φ_{sun} (Φ_{BB}) the solar spectrum (black body spectrum).⁴⁸ The SQ limit ($V_{\text{OC}}^{\text{RAD}} = V_{\text{OC}}^{\text{SQ}}$) corresponds to the case when $\text{EQE} = 1$ for $E > E_{\text{opt}}$, while $\text{EQE} = 0$ for $E < E_{\text{opt}}$. We note that, because of the different ideality factors, the contribution from deep trap states will be negligible under 1-sun conditions, as shown previously.¹⁴

As we have shown above, in low offset systems such as state-of-the-art NFA-based blends (or neat material systems), the CT absorption is mostly overshadowed by the stronger NFA absorption (or is absent). In such systems the sub-gap absorption tail is dominated by excitons ($\alpha = \alpha_{LE}$). The expected radiative limit V_{OC}^{RAD} set by excitons can be calculated by assuming $EQE = EQE_{max} \times (\alpha_{LE}/\alpha_{sat})$, with α_{LE} given by eq. (3). The concomitant radiative loss ΔV_{OC}^{RAD} , arising from the imperfect spectral line shape of α_{LE} (leading to deviations from the ideal box-like EQE shape), is shown in **Figure 5a** at different E_{opt} and σ_s . As shown, the voltage loss ΔV_{OC}^{RAD} increases with increasing σ_s . For example, when $\sigma_s = 100$ meV, ΔV_{OC}^{RAD} is larger than 0.2 V. Furthermore, at large σ_s , the voltage loss becomes more prominent at larger E_{opt} . We note that these losses are caused by a drastic increase in J_0^{RAD} , while J_{SC} is essentially unchanged. As σ_s is reduced, in turn, ΔV_{OC}^{RAD} is correspondingly decreased. For small static disorder (i.e., small σ_s), an analytical approximation relating ΔV_{OC}^{RAD} and σ_s can be obtained as

$$q\Delta V_{OC}^{RAD} \approx \frac{\sigma_s^2}{2kT} + kT \ln \left(\frac{E_{opt}}{3kT} \left[1 - \frac{\sigma_s^2}{2E_{opt}kT} \right]^3 \right). \quad (4)$$

A good agreement between eq. (4), as indicated by the dashed lines in Figure 5a, and the full simulation is indeed obtained for small σ_s . Importantly, even in the limit of vanishing static disorder, $\sigma_s \rightarrow 0$, a voltage loss ΔV_{OC}^{RAD} of roughly 70-80 meV is expected due to non-vanishing sub-gap absorption induced by thermal broadening (manifested by $\alpha \propto \exp(E/kT)$ in the gap). Based on the E_{opt} and σ_s extracted (see **Figure S11**) for the low-offset D:A systems PM6:Y6 ($E_{opt} = 1.44$ eV, $\sigma_s = 42$ meV), PM6:ITIC ($E_{opt} = 1.69$ eV, $\sigma_s = 37$ meV) and PBDB-T:EH-IDTBR ($E_{opt} = 1.77$ eV, $\sigma_s = 46$ meV), the radiative voltage loss induced by sub-gap absorption can be estimated. Subsequently, we find ΔV_{OC}^{RAD} of 108 mV for PM6:Y6, 107 mV for PM6:ITIC, and 120 mV for PBDB-T:EH-IDTBR. We note that the corresponding would-be ΔV_{OC}^{RAD} (if CT states were absent, see Fig. 4b) for PBDB-T:PC₇₀BM is 150 mV.

Finally, **Figure 5b** shows the corresponding effect of σ_s on the radiative limit of the PCE, assuming $EQE_{max} = 1$ (and ideal charge collection). Compared to the SQ limit of the PCE (indicated by black solid line), the presence of the sub-gap absorption results in a PCE peak loss of around 1.5 % for $\sigma_s = 0$. For $\sigma_s \neq 0$, the radiative PCE limit is further lowered, with the PCE peak decreasing with increasing σ_s . Hence, to minimize ΔV_{OC}^{RAD} , and thus maximize PCE, it is important to minimize σ_s . However, an unavoidable radiative loss, relative to the SQ limit, will still be present due to thermal broadening. Based on our findings, this loss is inherent to all organic solar cells, and needs to be taken into account in low offset systems where excitons dominate the sub-gap absorption.

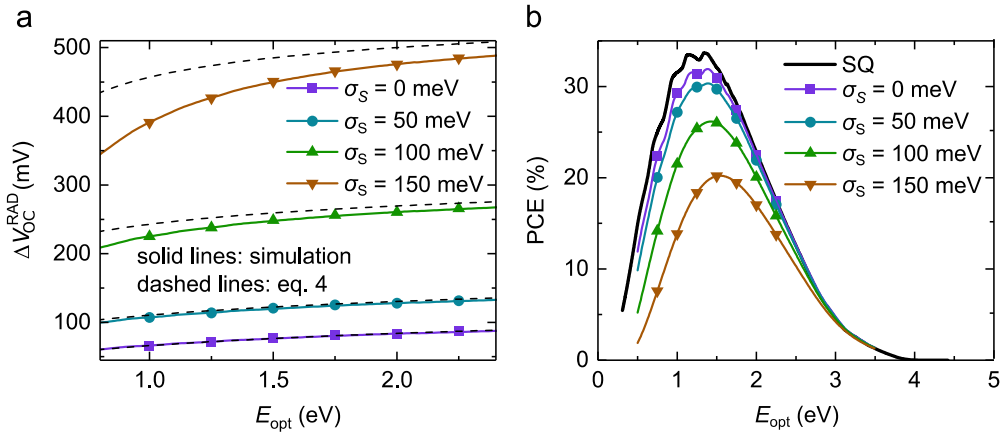


Figure 5 | The radiative V_{OC} loss induced by sub-gap absorption and associated radiative PCE limit of low-offset D:A solar cells. a, The radiative voltage loss ΔV_{OC}^{RAD} as a function of the optical bandgap for varying degree of Gaussian static disorder σ_s , assuming the sub-gap absorption dominated by LEs as per eq. 3 (solid lines with symbols). The corresponding analytical approximation (eq. 4) is represented by the dashed lines. **b,** The corresponding radiative PCE limit based on eq. 3, assuming $EQE_{max} = 1$ and ideal charge collection, is shown (solid lines with symbols). For comparison, the SQ limit, representing the ideal case with no sub-gap absorption, is included as indicated by the black solid line. The PCE decreases with respect to the SQ limit as σ_s increases. The SQ limit is not expected to be reached even for vanishing σ_s due to the thermal broadening.

Conclusion

In summary, we have shown that the exciton sub-gap absorption in organic semiconductors is dominated by Gaussian static disorder near the onset, while thermal broadening dominates at lower photon energies. Furthermore, we find that for a large number of organic semiconductors, the Urbach energy in the sub-gap absorption regime dominated by thermal broadening equals the thermal energy kT within the variations caused by the optical interference. While exponential absorption tails have been previously observed mainly in non-fullerene systems, we show that this property is universal for organic semiconductors and consistent with a Gaussian density of excitonic states undergoing Boltzmann-like thermally activated optical transitions. The static disorder is shown to arise from the width of the Gaussian DOS and to broaden the absorption onset at energies close to the optical gap. Using our model for the sub-gap excitonic absorption tail, it is possible to discriminate spectral regimes dominated by static disorder (where the Urbach energy is strongly dependent on the energy) and thermal broadening ($E_U = kT$), as well as to reproduce the temperature dependence of absorption coefficient due to excitons. This modified view of the sub-gap absorption coefficient in disordered organic semiconductors clarifies a longstanding debate concerning the shape of the DOS and the relevance of an Urbach description in these important and intriguing materials. Finally, we demonstrate the implications of exciton static disorder and thermal broadening on the radiative open-circuit voltage losses in organic solar cells based on low offset D:A blends.

Methods

Materials. PEDOT:PSS was purchased from Heraeus. Zinc acetate dihydrate and PCDTBT (Poly[N-9'-heptadecanyl-2,7-carbazole-alt-5,5-(4',7'-di-2-thienyl-2',1',3'-benzothiadiazole)]) were purchased from Sigma Aldrich. PC₇₀BM ([6,6]-Phenyl-C71-butyric acid methyl ester) and EH-IDTBR were purchased from Solarmer (Beijing). BQR (benzodithiophene-quaterthiophene-rhodanine) was provided by Prof. David. J Jones (University of Melbourne). m-MTDATA (4,4',4''-Tris[(3-methylphenyl)phenylamino]triphenylamine) was purchased from Ossila. IT-4F (3,9-bis(2-methylene-((3-(1,1-dicyanomethylene)-6,7-difluoro)-indanone))-5,5,11,11-tetrakis(4-hexylphenyl)-dithieno[2,3-d:2',3'-d']-s-indaceno[1,2-b:5,6-b']dithiophene), PM6 (Poly[(2,6-(4,8-bis(5-(2-ethylhexyl-3-fluoro)thiophen-2-yl)-benzo[1,2-b:4,5-b']dithiophene))-alt-(5,5-(1',3'-di-2-thienyl-5',7'-bis(2-ethylhexyl)benzo[1',2'-c:4',5'-c']dithiophene-4,8-dione))], Y6 (2,2'-((2Z,2'Z)-((12,13-bis(2-ethylhexyl)-3,9-diundecyl-12,13-dihydro-[1,2,5]thiadiazolo[3,4-e]thieno[2'',3'':4',5']thieno[2',3':4,5]pyrrolo[3,2-g]thieno[2',3':4,5]thieno[3,2-b]indole-2,10-diyl)bis(methanylylidene))bis(5,6-difluoro-3-oxo-2,3-dihydro-1H-indene-2,1-diylidene))dimalononitrile), ITIC (3,9-bis(2-methylene-(3-(1,1-dicyanomethylene)-indanone))-5,5,11,11-tetrakis(4-hexylphenyl)-dithieno[2,3-d:2',3'-d']-s-indaceno[1,2-b:5,6-b']dithiophene), PBDB-T (Poly[(2,6-(4,8-bis(5-(2-ethylhexyl)thiophen-2-yl)-benzo[1,2-b:4,5-b']dithiophene))-alt-(5,5-(1',3'-di-2-thienyl-5',7'-bis(2-ethylhexyl)benzo[1',2'-c:4',5'-c']dithiophene-4,8-dione))] and PTB7-Th (Poly[4,8-bis(5-(2-ethylhexyl)thiophen-2-yl)benzo[1,2-b:4,5-b']dithiophene-2,6-diyl-alt-(4-(2-ethylhexyl)-3-fluorothiopheno[3,4-b]thiophene-)-2-carboxylate-2,6-diyl])) were purchased from Zhi-yan (Nanjing) Inc.

Device Fabrication. Solar cells were fabricated with either a conventional architecture ITO/PEDOT:PSS/active layer/Ca/Al or inverted architecture ITO/ZnO/active layer/MoO₃/Ag. Commercial ITO coated glass substrates from Ossila were cleaned in an aqueous solution of Alconox at 60 °C, followed by an ultrasonic bath in deionize water, acetone and isopropanol. The cleaned substrates were dried with nitrogen, followed by a UV/O₃ treatment (Ossila, L2002A2-UK). For the conventional device architecture, 30 nm of PEDOT:PSS was spin-coated at 6000 rpm for 30 s onto precleaned ITO substrates and annealed at 155 °C for 15 min. As top electrode, 20 nm of calcium (Ca) and 100 nm of Aluminium (Al) were vacuum deposited at 10⁻⁶ Tor defining an active area of 4 mm². For the inverted device architecture with 30 nm of ZnO, a solution of 200 mg of zinc acetate dihydrate in 2-methoxyethanol (2 ml) and ethanolamine (56 µl) was prepared and stirred overnight under ambient conditions. The ZnO layer formed upon spin-coating the solution at 4000 rpm followed by thermal annealing at 200 °C for 60 min. As top electrode, 7 nm of MoO₃ and 100 nm of Ag were vacuum deposited at 10⁻⁶ Tor defining an active area of 4 mm².

Devices with conventional structure. BQR:PC₇₀BM devices were prepared using with the conventional architecture ITO/PEDOT:PSS/BQR:PC₇₀BM/Ca/Al. BQR and PC₇₀BM were dissolved in toluene (24 mg/ml with the donor:acceptor ratio of 1:1) and stirred at 60 °C for 3 hours. Next, the BQR:PC₇₀BM solution was spin-coated at 1000 rpm on the PEDOT:PSS layer to form a 100 nm thick film.

Devices with inverted structure. m-MTDATA:PC₇₀BM devices: Equimolar solutions of PC₇₀BM and m-MTDATA in dichloromethane (DCM) with a concentration of 19.4 mmol/l were prepared. To obtain a series of solutions with different molar ratios of m-MTDATA:PC₇₀BM (5 mol%, 1 mol%, 0.1 mol% and 0 mol% of m-MTDATA), 50 ul, 10 ul, 1 ul and 0 ul of m-MTDATA in DCM were added to 1 ml of PC₇₀BM in DCM. The solutions were spin-coated at a spin rate of 800 rpm to get an active layer thickness of around 90 nm. **PM6:Y6 devices:** PM6:Y6 was dissolved in CF solution (14 mg ml⁻¹ with 0.5 vol.% CN) with a donor:acceptor ratio of 1:1.2, and spin-coated (3000 rpm) on ZnO to form a 100 nm thick film. The casted active layers were thermally annealed at 110 °C for 10 min. **PM6:ITIC devices:** PM6:ITIC was dissolved in CB solution (18 mg ml⁻¹ with 0.5 vol.% DIO) with a donor:acceptor ratio of 1:1, and spin-coated (1000 rpm) on ZnO to form a 100 nm thick film. The active layers were further treated with thermal annealing at 100 °C for 10 min. **PBDB-T:EH-IDTBR devices:** PBDB-T:EH-IDTBR was dissolved in CB solution (14 mg ml⁻¹) with a donor:acceptor ratio of 1:1, and spin-coated (800 rpm) on ZnO to form a 100 nm thick film. **PBDB-T:ITIC devices:** PBDB-T:ITIC was dissolved in CB solution (14 mg ml⁻¹ with 0.5 vol.% DIO) with a donor:acceptor ratio of 1:1, and spin-coated (800 rpm) on ZnO to form a 100 nm thick film. The active layers were further treated with thermal annealing at 100 °C for 10 min. **PTB7-Th:ITIC devices:** PTB7-Th:ITIC was dissolved in CB solution (14 mg ml⁻¹ with 1 vol.% DIO) with a donor:acceptor ratio of 1:1.4, and spin-coated (1000 rpm) on ZnO to form a 100 nm thick film. **PBDB-T:PC₇₀BM devices:** PBDB-T:PC₇₀BM was dissolved in CB solution (14 mg ml⁻¹ with 3 vol.% DIO) with a donor:acceptor ratio of 1:1.4, and spin-coated (1000 rpm) on ZnO to form a 100 nm thick film. Then the as-cast films were rinsed with 80 µL of methanol at 4000 rpm for 20 s to remove the residual DIO. **PBDB-T:IT-4F devices:** PBDB-T:IT-4F was dissolved in CB solution (14 mg ml⁻¹ with 0.5 vol.% DIO) with a donor:acceptor ratio of 1:1, and spin-coated (800 rpm) on ZnO to form a 100 nm thick film. The active layers were further treated with thermal annealing at 100 °C for 10 min. **Neat ITIC devices:** ITIC was dissolved in chloroform solution (10 mg ml⁻¹) and spin-coated on ZnO (2000 rpm) to form a 70 nm thick film. **Neat IT-4F devices:** IT-4F was dissolved in chloroform solution (10 mg ml⁻¹) and spin-coated on ZnO (2000 rpm) to form a 70 nm thick film. **Neat PBDB-T devices:** PBDB-T was dissolved in chloroform solution (10 mg ml⁻¹) and spin-coated on ZnO (3000 rpm) to form a 70 nm thick film.

EQE measurements. A homebuilt setup including a Perkin Elmer UV/VIS/NIR spectrometer (LAMBDA 950) as a source for monochromatic light was used. The light was chopped at 273 Hz and

directed onto the device under test (DUT). The resulting photocurrent was amplified by a low noise current amplifier (FEMTO DLPCA-200) and measured with the Stanford SR860 lock-in amplifier. To decrease the noise floor of the setup, the DUT was mounted in an electrically shielded and temperature controlled Linkam sample stage. An integration time up to 1000 seconds was used for detecting wavelengths above 1500 nm. NIST-calibrated silicon and GaAs photodiodes from Newport were used as a calibration reference. The temperature inside the Linkam sample stage was set to -120 to 60 °C by the Linkam T96 temperature controller in combination with an LNP96 liquid nitrogen pump. The commercial amorphous silicon thin film solar cell, used for temperature dependent EQE measurements, was manufactured by TRONY with the part number sc80125s-8.

Gaussian fits. The EQE associated with CT states and mid-gap states were routinely fitted in accordance with the standard Marcus charge-transfer formalism. The associated EQEs are given by $\text{EQE}_{\text{CT}}(E) = g(E, E_{\text{CT}}, \lambda_{\text{CT}}, f_{\text{CT}})$ and $\text{EQE}_{\text{t}}(E) = g(E, E_{\text{t}}, \lambda_{\text{t}}, f_{\text{t}})$ for CT and mid-gap state absorption, respectively, where

$$g(E, E_j, \lambda_j, f_j) = f_j E^{-1} (4\pi\lambda_j kT)^{-\frac{1}{2}} \exp\left(-\frac{(E_j + \lambda_j - E)^2}{4\lambda_j kT}\right). \quad (5)$$

Here, f_j , E_j and λ_j are fitting parameters. All fit parameters obtained in this work are summarized in **Table S1**. The EQEs are assumed to be related to their respective absorption coefficients as $\alpha_{\text{CT}}(E) \propto \text{EQE}_{\text{CT}}(E)$ and $\alpha_{\text{t}}(E) \propto \text{EQE}_{\text{t}}(E)$ (neglecting interference effects).

Data Availability

The data that support the findings of this study are available from the corresponding author upon reasonable request.

References

- (1) Zhao, W.; Li, S.; Yao, H.; Zhang, S.; Zhang, Y.; Yang, B.; Hou, J. Molecular Optimization Enables over 13% Efficiency in Organic Solar Cells. *J. Am. Chem. Soc.* **2017**, *139* (21), 7148–7151. <https://doi.org/10.1021/jacs.7b02677>.
- (2) Jin, K.; Xiao, Z.; Ding, L. 18.69% PCE from Organic Solar Cells. *J. Semicond.* **2021**, *42* (6), 060502. <https://doi.org/10.1088/1674-4926/42/6/060502>.
- (3) Urbach, F. The Long-Wavelength Edge of Photographic Sensitivity and of the Electronic Absorption of Solids. *Phys. Rev.* **1953**, *92* (5), 1324. <https://doi.org/10.1103/PhysRev.92.1324>.
- (4) Cody, G. D.; Tiedje, T.; Abeles, B.; Brooks, B.; Goldstein, Y. Disorder and the Optical-

- Absorption Edge of Hydrogenated Amorphous Silicon. *Phys. Rev. Lett.* **1981**, *47* (20), 1480–1483. <https://doi.org/10.1103/PhysRevLett.47.1480>.
- (5) Bonalde, I.; Medina, E.; Rodríguez, M.; Wasim, S. M.; Marín, G.; Rincón, C.; Rincón, A.; Torres, C. Urbach Tail, Disorder, and Localized Modes in Ternary Semiconductors. *Phys. Rev. B - Condens. Matter Mater. Phys.* **2004**, *69* (19), 1–5. <https://doi.org/10.1103/PhysRevB.69.195201>.
- (6) Bansal, B.; Dixit, V. K.; Venkataraman, V.; Bhat, H. L. Alloying Induced Degradation of the Absorption Edge of in As XSb_{1-X}. *Appl. Phys. Lett.* **2007**, *90* (10). <https://doi.org/10.1063/1.2711388>.
- (7) Pankove, J. I. Absorption Edge of Impure Gallium Arsenide. *Phys. Rev.* **1965**, *140* (6A). <https://doi.org/10.1103/PhysRev.140.A2059>.
- (8) Kurik, M. V. Urbach Rule. *Phys. Status Solidi* **1971**, *8* (1), 9–45. <https://doi.org/10.1002/pssa.2210080102>.
- (9) Grein, C. H.; John, S. Temperature Dependence of the Urbach Optical Absorption Edge: A Theory of Multiple Phonon Absorption and Emission Sidebands. *Phys. Rev. B* **1989**, *39* (2), 1140–1151. <https://doi.org/10.1103/PhysRevB.39.1140>.
- (10) Corkish, R.; Green, M. A. Band Edge Optical Absorption in Intrinsic Silicon: Assessment of the Indirect Transition and Disorder Models (Journal of Applied Physics (1993) 73 (3988)). *J. Appl. Phys.* **1993**, *74* (10), 6462. <https://doi.org/10.1063/1.355344>.
- (11) Dow, J. D.; Redfield, D. Toward a Unified Theory of Urbach's Rule and Exponential Absorption Edges. *Phys. Rev. B* **1972**, *5* (2), 594–610. <https://doi.org/10.1017/CBO9781107415324.004>.
- (12) Shklovskii, B. I.; Efros, A. L. *Electronic Properties of Doped Semiconductors*; Springer Series in Solid-State Sciences; Springer Berlin Heidelberg: Berlin, Heidelberg, 1984; Vol. 45. <https://doi.org/10.1007/978-3-662-02403-4>.
- (13) Rahimi, K.; Botiz, I.; Agumba, J. O.; Motamen, S.; Stingelin, N.; Reiter, G. Light Absorption of Poly(3-Hexylthiophene) Single Crystals. *RSC Adv.* **2014**, *4* (22), 11121–11123. <https://doi.org/10.1039/c3ra47064d>.
- (14) Zarrabi, N.; Sandberg, O. J.; Zeiske, S.; Li, W.; Riley, D. B.; Meredith, P.; Armin, A. Charge-Generating Mid-Gap Trap States Define the Thermodynamic Limit of Organic Photovoltaic Devices. *Nat. Commun.* **2020**, *11* (1), 5567. <https://doi.org/10.1038/s41467-020-19434-0>.
- (15) Vandewal, K.; Tvingstedt, K.; Gadisa, A.; Inganäs, O.; Manca, J. V. Relating the Open-Circuit

- Voltage to Interface Molecular Properties of Donor:Acceptor Bulk Heterojunction Solar Cells. *Phys. Rev. B - Condens. Matter Mater. Phys.* **2010**, *81* (12), 1–8.
<https://doi.org/10.1103/PhysRevB.81.125204>.
- (16) Burke, T. M.; Sweetnam, S.; Vandewal, K.; McGehee, M. D. Beyond Langevin Recombination : How Equilibrium Between Free Carriers and Charge Transfer States Determines the Open-Circuit Voltage of Organic Solar Cells. *Adv. Energy Mater.* **2015**, *1500123*, 1–12. <https://doi.org/10.1002/aenm.201500123>.
- (17) Kahle, F. J.; Rudnick, A.; Bäessler, H.; Köhler, A. How to Interpret Absorption and Fluorescence Spectra of Charge Transfer States in an Organic Solar Cell. *Mater. Horizons* **2018**, *5* (5), 837–848. <https://doi.org/10.1039/c8mh00564h>.
- (18) Tvingstedt, K.; Benduhn, J.; Vandewal, K. Temperature Dependence of the Spectral Line-Width of Charge-Transfer State Emission in Organic Solar Cells; Static vs. Dynamic Disorder. *Mater. Horizons* **2020**, *7* (7), 1888–1900. <https://doi.org/10.1039/D0MH00385A>.
- (19) Felekidis, N.; Melianas, A.; Kemerink, M. The Role of Delocalization and Excess Energy in the Quantum Efficiency of Organic Solar Cells and the Validity of Optical Reciprocity Relations. *J. Phys. Chem. Lett.* **2020**, *11* (9), 3563–3570.
<https://doi.org/10.1021/acs.jpcllett.0c00945>.
- (20) Qian, D.; Zheng, Z.; Yao, H.; Tress, W.; Hopper, T. R.; Chen, S.; Li, S.; Liu, J.; Chen, S.; Zhang, J.; Liu, X. K.; Gao, B.; Ouyang, L.; Jin, Y.; Pozina, G.; Buyanova, I. A.; Chen, W. M.; Inganäs, O.; Coropceanu, V.; Bredas, J. L.; Yan, H.; Hou, J.; Zhang, F.; Bakulin, A. A.; Gao, F. Design Rules for Minimizing Voltage Losses in High-Efficiency Organic Solar Cells. *Nat. Mater.* **2018**, *17* (8), 703–709. <https://doi.org/10.1038/s41563-018-0128-z>.
- (21) Ran, N. A.; Love, J. A.; Takacs, C. J.; Sadhanala, A.; Beavers, J. K.; Collins, S. D.; Huang, Y.; Wang, M.; Friend, R. H.; Bazan, G. C.; Nguyen, T. Q. Harvesting the Full Potential of Photons with Organic Solar Cells. *Adv. Mater.* **2016**, *28* (7), 1482–1488.
<https://doi.org/10.1002/adma.201504417>.
- (22) Liu, S.; Yuan, J.; Deng, W.; Luo, M.; Xie, Y.; Liang, Q.; Zou, Y. High-Efficiency Organic Solar Cells with Low Non-Radiative Recombination Loss and Low Energetic Disorder. *Nat. Photonics* **2020**, *in press*. <https://doi.org/10.1038/s41566-019-0573-5>.
- (23) Jain, N.; Chandrasekaran, N.; Sadhanala, A.; Friend, R. H.; McNeill, C. R.; Kabra, D. Interfacial Disorder in Efficient Polymer Solar Cells: The Impact of Donor Molecular Structure and Solvent Additives. *J. Mater. Chem. A* **2017**, *5* (47), 24749–24757.
<https://doi.org/10.1039/c7ta07924a>.

- (24) Bäessler, H. Charge Transport in Disordered Organic Photoconductors a Monte Carlo Simulation Study. *Phys. Status Solidi* **1993**, *175* (1), 15–56.
<https://doi.org/10.1002/pssb.2221750102>.
- (25) Beenken, W. J. D.; Herrmann, F.; Presselt, M.; Hoppe, H.; Shokhovets, S.; Gobsch, G.; Runge, E. Sub-Bandgap Absorption in Organic Solar Cells: Experiment and Theory. *Phys. Chem. Chem. Phys.* **2013**, *15* (39), 16494–16502. <https://doi.org/10.1039/c3cp42236d>.
- (26) Blakesley, J. C.; Neher, D. Relationship between Energetic Disorder and Open-Circuit Voltage in Bulk Heterojunction Organic Solar Cells. *Phys. Rev. B - Condens. Matter Mater. Phys.* **2011**, *84* (7). <https://doi.org/10.1103/PhysRevB.84.075210>.
- (27) Kaiser, C.; Zeiske, S.; Meredith, P.; Armin, A. Determining Ultralow Absorption Coefficients of Organic Semiconductors from the Sub-Bandgap Photovoltaic External Quantum Efficiency. *Adv. Opt. Mater.* **2019**, *8* (1), 1901542.
<https://doi.org/https://doi.org/10.1002/adom.201901542>.
- (28) Armin, A.; Zarrabi, N.; Sandberg, O. J.; Kaiser, C.; Zeiske, S.; Li, W.; Meredith, P. Limitations of Charge Transfer State Parametrisation and Relevance for Non-Fullerene Acceptors. *Adv. Energy Mater.* **2020**, *in press*. <https://doi.org/10.1002/aenm202001828>.
- (29) Armin, A.; Kassal, I.; Shaw, P. E.; Hambsch, M.; Stolterfoht, M.; Lyons, D. M.; Li, J.; Shi, Z.; Burn, P. L.; Meredith, P. Spectral Dependence of the Internal Quantum Efficiency of Organic Solar Cells: Effect of Charge Generation Pathways. *J. Am. Chem. Soc.* **2014**, *136* (32), 11465–11472. <https://doi.org/10.1021/ja505330x>.
- (30) Vandewal, K.; Albrecht, S.; Hoke, E. T.; Graham, K. R.; Widmer, J.; Douglas, J. D.; Schubert, M.; Mateker, W. R.; Bloking, J. T.; Burkhard, G. F.; Sellinger, A.; Frechet, J. M.; Amassian, A.; Riede, M. K.; McGehee, M. D.; Neher, D.; Salleo, A. Efficient Charge Generation by Relaxed Charge-Transfer States at Organic Interfaces. *Nat. Mater.* **2014**, *13* (1), 63–68.
<https://doi.org/10.1038/nmat3807>.
- (31) Kurpiers, J.; Ferron, T.; Roland, S.; Jakoby, M.; Thiede, T.; Jaiser, F.; Albrecht, S.; Janietz, S.; Collins, B. A.; Howard, I. A.; Neher, D. Probing the Pathways of Free Charge Generation in Organic Bulk Heterojunction Solar Cells. *Nat. Commun.* **2018**, *9* (1), 1–11.
<https://doi.org/10.1038/s41467-018-04386-3>.
- (32) Lee, J.; Vandewal, K.; Yost, S. R.; Bahlke, M. E.; Goris, L.; Baldo, M. A.; Manca, J. V.; Voorhis, T. Van. Charge Transfer State versus Hot Exciton Dissociation in Polymer-Fullerene Blended Solar Cells. *J. Am. Chem. Soc.* **2010**, *132* (34), 11878–11880.
<https://doi.org/10.1021/ja1045742>.

- (33) Sandberg, O. J.; Zeiske, S.; Zarrabi, N.; Meredith, P.; Armin, A. Charge Carrier Transport and Generation via Trap-Mediated Optical Release in Organic Semiconductor Devices. *Phys. Rev. Lett.* **2020**, *124* (12), 128001. <https://doi.org/10.1103/PhysRevLett.124.128001>.
- (34) Gielen, S.; Kaiser, C.; Verstraeten, F.; Kublitski, J.; Benduhn, J.; Spoltore, D.; Verstappen, P.; Maes, W.; Meredith, P.; Armin, A.; Vandewal, K. Intrinsic Detectivity Limits of Organic Near-Infrared Photodetectors. *Adv. Mater.* **2020**, *32* (47), 2003818. <https://doi.org/10.1002/adma.202003818>.
- (35) Nikolis, V. C.; Mischok, A.; Siegmund, B.; Kublitski, J.; Jia, X.; Benduhn, J.; Hörmann, U.; Neher, D.; Gather, M. C.; Spoltore, D.; Vandewal, K. Strong Light-Matter Coupling for Reduced Photon Energy Losses in Organic Photovoltaics. *Nat. Commun.* **2019**, *10* (1), 1–8. <https://doi.org/10.1038/s41467-019-11717-5>.
- (36) Göhler, C.; Saladina, M.; Wang, Y.; Spoltore, D.; Benduhn, J.; Leo, K.; Deibel, C. Temperature Dependent Charge Transfer State Absorption and Emission Reveal Dominant Role of Dynamic Disorder in Organic Solar Cells. **2021**, arXiv:2102.06071v1.
- (37) Searle, T. M.; Jackson, W. A. Static versus Electron-Phonon Disorder in Amorphous Si: H and Its Alloys. *Philos. Mag. B Phys. Condens. Matter; Stat. Mech. Electron. Opt. Magn. Prop.* **1989**, *60* (2), 237–255. <https://doi.org/10.1080/13642818908211192>.
- (38) Cody, G. D. Urbach Edge of Crystalline and Amorphous Silicon: A Personal Review. *J. Non. Cryst. Solids* **1992**, *141* (C), 3–15. [https://doi.org/10.1016/S0022-3093\(05\)80513-7](https://doi.org/10.1016/S0022-3093(05)80513-7).
- (39) Leblanc, F. Related Content Accurate Determination of the Urbach Energy of A- Si : H Thin Films by Correction for the Interference Effect. *Japanese J. Appl. Phys. Jpn. J. Appl. Phys* **1994**, *33*, 1755–1758. <https://doi.org/10.1143/jjap.33.11755>.
- (40) Tang, J. Electron-Transfer Reactions Involving Non-Linear Spin-Boson Interactions. *Chem. Phys.* **1994**, *188* (2–3), 143–160. [https://doi.org/10.1016/0301-0104\(94\)00254-1](https://doi.org/10.1016/0301-0104(94)00254-1).
- (41) Casado-pascual, J.; Morillo, M.; Goychuk, I.; Hänggi, P.; Morillo, M. The Role of Different Reorganization Energies within the Zusman Theory of Electron Transfer The Role of Different Reorganization Energies within the Zusman Theory of Electron Transfer. *J. Chem. Phys.* **2003**, *118* (1), 291. <https://doi.org/10.1063/1.1525799>.
- (42) Keil, T. H. Theory of the Urbach Rule. *Phys. Rev.* **1966**, *144* (2), 582–587. <https://doi.org/10.1103/PhysRev.144.582>.
- (43) Hood, S.; Zarrabi, N.; Meredith, P.; Kassal, I.; Armin, A. Measuring Energetic Disorder in Organic Semiconductors Using the Photogenerated Charge-Separation Efficiency. *J. Phys.*

- Chem. Lett.* **2019**, *10* (14), 3863–3870. <https://doi.org/10.1021/acs.jpcclett.9b01304>.
- (44) Miller, A.; Abrahams, E. Impurity Conduction at Low Concentrations. *Phys. Rev.* **1960**, *120* (3), 745–755. <https://doi.org/10.1103/PhysRev.120.745>.
- (45) Cui, Y.; Yao, H.; Zhang, J.; Xian, K.; Zhang, T.; Hong, L.; Wang, Y.; Xu, Y.; Ma, K.; An, C.; He, C.; Wei, Z.; Gao, F.; Hou, J. Single-Junction Organic Photovoltaic Cells with Approaching 18% Efficiency. *Adv. Mater.* **2020**, *32* (19), 1–7. <https://doi.org/10.1002/adma.201908205>.
- (46) Song, B.; Rolin, C.; Zimmerman, J. D.; Forrest, S. R. Effect of Mixed Layer Crystallinity on the Performance of Mixed Heterojunction Organic Photovoltaic Cells. *Adv. Mater.* **2014**, *26* (18), 2914–2918. <https://doi.org/10.1002/adma.201305099>.
- (47) Venkateshvaran, D.; Nikolka, M.; Sadhanala, A.; Lemaur, V.; Zelazny, M.; Kepa, M.; Hurhangee, M.; Kronemeijer, A. J.; Pecunia, V.; Nasrallah, I.; Romanov, I.; Broch, K.; McCulloch, I.; Emin, D.; Olivier, Y.; Cornil, J.; Beljonne, D.; Sirringhaus, H. Approaching Disorder-Free Transport in High-Mobility Conjugated Polymers. *Nature* **2014**, *515* (7527), 384–388. <https://doi.org/10.1038/nature13854>.
- (48) Shockley, W.; Queisser, H. J. Detailed Balance Limit of Efficiency of P-n Junction Solar Cells. *J. Appl. Phys.* **1961**, *32* (3), 510–519. <https://doi.org/10.1063/1.1736034>.

Acknowledgements

This work was funded through the Welsh Government’s Sêr Cymru II Program ‘Sustainable Advanced Materials’ (Welsh European Funding Office – European Regional Development Fund). C.K. is recipient of a UKRI EPSRC Doctoral Training Program studentship. N.Z. is funded by a studentship through the Sêr Cymru II Program. P.M. is a Sêr Cymru II Research Chair and A.A. is a Rising Star Fellow also funded through the Welsh Government’s Sêr Cymru II ‘Sustainable Advanced Materials’ Program (European Regional Development Fund, Welsh European Funding Office and Swansea University Strategic Initiative).

Author Contributions

AA and PM provided the overall leadership of the project. OJS and AA conceptualised the idea. CK and AA designed the experiments. CK performed most measurements, analysed the data, performed optical modelling and drafted the manuscript. OJS developed the theoretical model. CK, OJS and AA interpreted the data. NZ assisted with EQE_{PV} measurements. WL fabricated the devices. All co-authors contributed in the development of the manuscript which was initially drafted by CK.

Additional information

Supplementary Information

Competing interests: The authors declare no competing interests.